"Looking Through Walls" – Actuator Position Measurement Through a Conductive Wall

R. Giuffrida,
S. Miric,
D. Bortis,
J. W. Kolar

ETH
Eidgenössische Technische Hochschule Zürich
Swiss Federal Institute of Technology Zurich

"Looking Through Walls" – Actuator Position Measurement Through a Conductive Wall

Rosario V. Giuffrida, Spasoje Mirić, Dominik Bortis and Johann W. Kolar

Power Electronic Systems Laboratory, ETH Zurich, Zurich, Switzerland

giuffrida@lem.ee.ethz.ch

Abstract—**This paper investigates the design of an Eddy Current Sensor (ECS) for position measurement of a moving conductive target located behind a fixed conductive shielding surface. Such a sensor can e.g. be used in completely sealed actuators with magnetically levitated rotor or mover for high purity applications. A detailed analysis of the sensor is conducted, starting from the conventional ECS and its equivalent circuit model, which is then further extended to an ECS looking through a conductive wall. With the aid of Finite Element Methods (FEM) simulations, a deeper understanding of the sensor operating principle is provided, together with guidelines to select its optimal excitation frequency, based on the properties of the selected materials for the target and the shielding surface. A sensitivity analysis is then conducted and the results are finally verified with measurements on a hardware sensor prototype, showing that the sensor can be used to capture the mover position in an active magnetic bearing control structure.**

I. INTRODUCTION

In many industrial applications of actuators a contactless position sensing of an object is of main importance. In the case of a conductive object, a popular choice are Eddy Current Sensors (ECSs), which due to their non-contact nature offer a clear advantage over e.g. resistive or capacitive sensors [1]. Moreover, ECSs can also operate under harsh conditions, in dirty environments or in vacuum, which makes them suitable for many different applications for the stationary, quasi-stationary [2] or dynamic position measurement [3] in the nm- to mm-range, e.g. in Magnetic Bearings (MBs) of actuator systems employing magnetic levitation [4]–[6], where the ECSs located on the stator are used to capture the position of the levitated rotor or mover (cf. **Fig. 1 (a)**). Besides position sensing, ECSs are also extensively used in non-destructive testing for inspection of irregularities or damages on the surface of conductive materials [7]. Typically, ECSs are either realized as a single- or dual coil configuration, where either the distance-dependent variation of the excitation coil impedance or the distance-dependent induced voltage in a second pick-up coil is measured. The design of such single- and dual-coil ECSs is thoroughly discussed in the literature [8]–[11].

In contrast, there are also applications where the moving conductive target is located behind another conductive material. For example, in entirely sealed actuator systems used for high purity food, medical or chemical applications, the stator and the magnetically levitated mover are fully encapsulated e.g. with a stainless steel housing (cf. **Fig. 1 (b)**). Consequently, the ECS located on the stator has to measure the mover's position through the stainless steel cover of the stator, which due to its conductivity highly degrades the magnetic coupling between excitation and/or pick-up coil and the mover, and in turn leads to a reduction of the measurement sensitivity, i.e. mover position accuracy.

In the literature, such an ECS measuring through a conductive wall is e.g. described in [12], where a commercially available eddy current flaw detector is used for periodical inspections of nuclear power plants by measuring the distance between two conductive tubes. There, the well established Dodd and Deeds analytic models [13], [14] are validated with measurements, and sensitivity results of the sensor output are given for different excitation frequencies up to 16 kHz. For stationary applications, such low excitation frequencies are clearly sufficient, however, for an ECS designed for the dynamic position measurement in entirely sealed MBs this results in a too low measurement bandwidth. In order to achieve a position control bandwidth of around 1-2 kHz, sensor measurement bandwidths of at
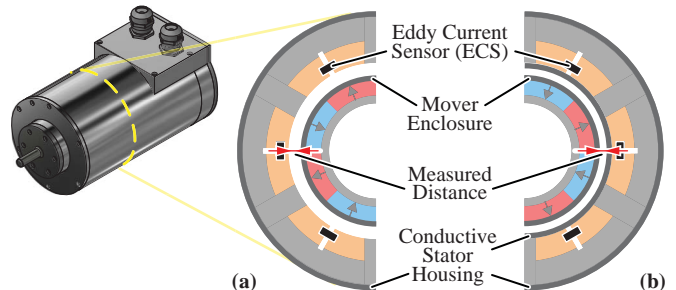
Fig. 1: 3D-view and corresponding cross section view of a magnetically levitated rotary-linear actuator system showing the placement of the Eddy Current Sensors (ECSs) for **(a)** a non-sealed actuator version, where conventional ECSs are applicable and **(b)** a sealed actuator version, where the ECS has to measure the mover position through the conductive stator housing.

TABLE I: ECS Specifications defined by the underlying application.

Parameter	Value	Unit
Measurable Distance δ	$0 \ldots 2$	[mm]
Sensor Resolution	1-10	[µm]
Sensor Bandwidth f_{bw}	10-20	[kHz]
Max. ECS Coil Diameter d_{c}	11.5	[mm]
Enclosure Thickness (Stator and Mover)	$0.2 \ldots 0.5$	[mm]
Enclosure Material (Stator and Mover)	Stainless Steel	

least 10-20 kHz are needed [4], [6], which again roughly lead to 10 times higher excitation frequencies of above 100-200 kHz.

However, for ECS looking through a conductive wall, it also has to be considered that above a certain excitation frequency - defined by the material properties and dimensions of the intermediate layer - the skin and proximity effects of this layer start to play an important role and in the worst case can lead to a complete loss of any mover position information. Consequently, the ECS's excitation frequency has to be selected properly, such that on the one hand a sufficient position measurement bandwidth is achieved, and on the other hand the position sensitivity is not too much affected by the intermediate conductive layer.

Therefore, this paper aims to provide a general understanding and design guidelines of the ECS measuring through a conductive layer, i.e. how the applicable excitation frequency range is influenced by the material properties and dimensions of both the intermediate layer and the mover, and how the frequency is optimally selected to achieve the highest position sensitivity. The presented FEM simulation based analysis is conducted for an ECS used as position sensor of the aforementioned entirely sealed linear-rotary actuator systems with magnetically levitated mover, whose specifications are given in **Tab. I**. Even though for this application the stator and mover materials are already defined, the influence of other sealing materials is investigated. The paper is structured as follows. **Sec. II** starts from the basic operating principle of a conventional ECS, where based on an equivalent transformer model and corresponding FEM simulations it is shown how the minimum applicable excitation frequency is influenced by the mover's material properties and dimensions. Afterwards, in **Sec. III**, the influence of a conductive intermediate layer is analyzed with FEM simulations for different material combinations and an upper limit for the excitation frequency is given. Furthermore, a sensitivity analysis is conducted, in order to define the optimal operating frequency
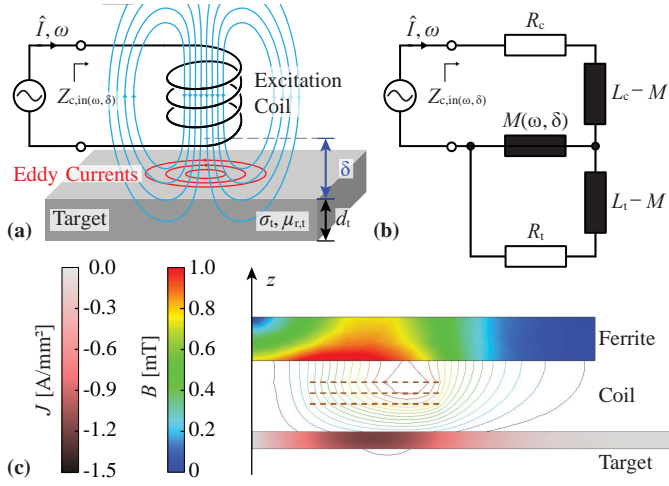
Fig. 2: (a) Structure of a conventional planar single-coil ECS to measure the distance δ between the stationary excitation coil and the moveable target. (b) Transformer equivalent circuit with coil and target self-inductances L_c and L_t as well as the frequency- and distance-dependent mutual inductance $M(\omega, \delta)$. (c) ECS arrangement used for the axisymmetrical 2D FEM simulations (ANSYS) with exemplary field and current distribution for a 0.5 mm stainless steel target at an excitation frequency of $f_\mathrm{exc} = 430\,\mathrm{kHz}$.

range for the selected materials. With the provided guidelines, then in **Sec. IV** the hardware setup with the excitation coil design, the measurement circuit and the test bench are discussed, while in **Sec. V** impedance measurements of the realized hardware prototypes are compared with the previously performed FEM simulations. In addition, the optimal excitation frequencies are deduced for different material combinations and the corresponding sensitivities are listed, from which the achievable position accuracies can be calculated. Finally, **Sec. VI** concludes the paper.

II. OPERATING PRINCIPLE OF THE CONVENTIONAL ECS

In general, as shown in **Fig. 2 (a)** for a simplified planar structure, a single-coil ECS consists of a *stationary excitation coil* which is placed at a certain distance δ from a *moving target* with specific conductivity σ_t, relative permeability $\mu_\mathrm{r,t}$ and thickness d_t. Since in many applications a paramagnetic material as e.g. stainless steel, copper or aluminum is selected for the target, in the following a permeability of $\mu_\mathrm{r,t} \approx 1$ is assumed.

The coil is typically excited with a high-frequency AC current, generating a surrounding magnetic field H_c which also penetrates the moving target. Hence, the high-frequency magnetic flux linked with the target induces a voltage in the target and, due to the target's conductivity σ_t, it leads to eddy currents circulating in the target, which generate a second magnetic field H_t counteracting the magnetic field of the coil. For a fixed excitation frequency and given material properties of the target, the intensity of this interaction, i.e. the magnetic coupling between coil and target, only depends on the distance δ, which for a single-coil ECS configuration finally reflects into a measurable change of the coil's input impedance $Z_\mathrm{c,in}(\omega, \delta)$. Hence, by knowing the relation between δ and the variation of the coil input resistance and/or inductance, the position of the target is accurately measurable. Instead of measuring this distance-dependent impedance variation, in a dual-coil ECS configuration a second stationary pickup coil is used, where a distance-dependent induced voltage is measured. However, in this paper only the single-coil ECS is considered, since the findings are also directly applicable to the dual-coil ECS configuration, as the induced voltage variation is directly related to the inductance variation.

A. Equivalent Transformer Model

For the conventional single-coil ECS, the impedance variation of the excitation coil can be described by an equivalent transformer model as shown in **Fig. 2 (b)**, where R_c and L_c are the (DC) resistance

and inductance of the excitation coil, R_t and L_t are the resistance and inductance of the target, ω denominates the angular excitation frequency and $M = k\sqrt{L_\mathrm{c}L_\mathrm{t}}$ the mutual inductance between coil and target, with the coupling factor k. Both the mutual inductance M and the coupling factor k depend on the angular frequency ω and the distance δ, i.e. $M = M(\omega, \delta)$ and $k = k(\omega, \delta)$. Hence, for a given ECS setup, the excitation frequency $f_\mathrm{exc} = \omega_\mathrm{exc}/2\pi$ is selected in such a way that on the one hand a high measurement sensitivity and on the other hand a large enough measurement bandwidth is achieved. The measurement sensitivity is proportional to the variation of the coil's input impedance $Z_\mathrm{c,in}$, which can be split into an equivalent input resistance $R_\mathrm{c,in}$ (real part) and inductance $L_\mathrm{c,in}$ (imaginary part, divided by ω), which according to the equivalent model are expressed as

$$R_\mathrm{c,in} = R_\mathrm{c} + \frac{\omega^2 M^2}{R_\mathrm{t}^2 + \omega^2 L_\mathrm{t}^2}\, R_\mathrm{t} = R_\mathrm{c} + R_\mathrm{c,var}(\omega, \delta), \qquad (1)$$

$$L_\mathrm{c,in} = L_\mathrm{c} - \frac{\omega^2 M^2}{R_\mathrm{t}^2 + \omega^2 L_\mathrm{t}^2}\, L_\mathrm{t} = L_\mathrm{c} + L_\mathrm{c,var}(\omega, \delta). \qquad (2)$$

As can be noticed, for low angular frequencies ω, the variable parts $R_\mathrm{c,var}(\omega, \delta)$ and $L_\mathrm{c,var}(\omega, \delta)$ vanish, and a distance-independent impedance $Z_\mathrm{c,in} = R_\mathrm{c} + j\omega L_\mathrm{c}$ given by the coil resistance and its self-inductance is measured.

Hence, the excitation frequency has to be selected above a certain lower frequency limit, which is defined by a *coupling-independent* angular cutoff frequency

$$\omega_\mathrm{co} = 2\pi f_\mathrm{co} = R_\mathrm{t}/L_\mathrm{t}, \qquad (3)$$

since around this frequency (± 1 decade) the input resistance increases by

$$R_\mathrm{c,var}(\omega, \delta) = \left(\frac{M}{L_\mathrm{t}}\right)^2 R_\mathrm{t} = k(\omega, \delta)^2 L_\mathrm{c}\omega_\mathrm{co}, \qquad (4)$$

while the input inductance decreases by

$$L_\mathrm{c,var}(\omega, \delta) = -\left(\frac{M^2}{L_\mathrm{t}}\right) = -k(\omega, \delta)^2 L_\mathrm{c}. \qquad (5)$$

Accordingly, for a selected excitation frequency f_exc around or above f_co, the resistance as well as the inductance variation can be used to measure the distance δ between target and coil. In this case, the coupling factor $k(f_\mathrm{exc}, \delta)$ only depends on δ and thus for larger δ, i.e. lower $k(f_\mathrm{exc}, \delta)$, the measured resistance $R_\mathrm{c,in}$ decreases, while the measured inductance $L_\mathrm{c,in}$ increases. Furthermore, it is interesting to note that ω_co can be modified by the target material and thickness, i.e. the target resistance R_t, and the dimensions of the ECS, since L_t scales proportionally to the coil's self-inductance L_c. Consequently, for a given ECS geometry, a target material with higher conductivity σ_t or larger thickness d_t shifts ω_co to lower frequencies and in cases where the inductance variation is measured, either a lower f_exc could be selected or a higher sensitivity can be achieved. In case of resistance variation, however, a lower R_t also means lower sensitivity.

B. Impedance Variation obtained by FEM Simulations

Fig. 3 shows these relationships between cutoff frequency f_co, resistance and inductance variation $R_\mathrm{c,var}(\omega, \delta)$ and $L_\mathrm{c,var}(\omega, \delta)$ for a fixed target thickness of $0.5\,\mathrm{mm}$ and two different materials, i.e. stainless steel and aluminum. The distance δ is gradually increased between $0\,\mathrm{mm}$ (min. position), $1\,\mathrm{mm}$ (nom. position) and $2\,\mathrm{mm}$ (max. position), whereas here - for the conventional ECS without intermediate conductive layer - an offset of $0.5\,\mathrm{mm}$ has to be considered, which means that for $\delta = 0\,\mathrm{mm}$ the effective distance between coil and target is $0.5\,\mathrm{mm}$. The impedance curves of **Fig. 3** are obtained from axisymmetrical 2D FEM simulations (ANSYS) for the ECS structure shown in **Fig. 2 (c)**, whose excitation coil design is discussed in **Sec. IV-A**.

As can be noticed from **Fig. 3**, since aluminum has an approximately 26 times higher conductivity than stainless steel, its cutoff frequency
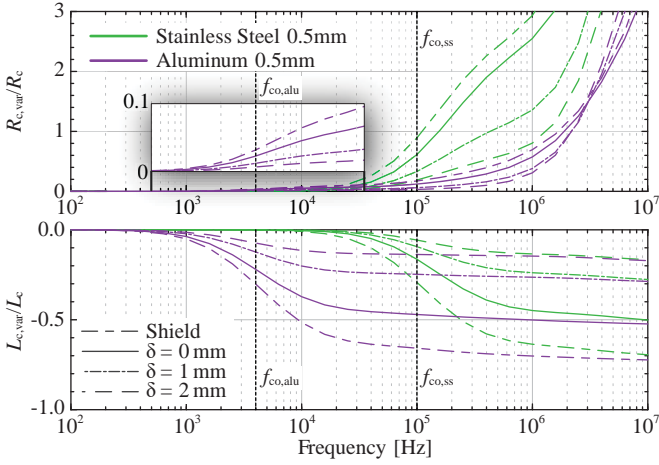
Fig. 3: Normalized variable parts $R_{c,var}(\omega, \delta)$ and $L_{c,var}(\omega, \delta)$ versus frequency for stainless steel and aluminum target ($d_t = 0.5\,mm$) at $\delta = 0\,mm$, $1\,mm$ and $2\,mm$, obtained from FEM simulations (cf. **Fig. 2 (c)**).

$f_{co,alu}$ as well as its resistance sensitivity $R_{c,alu}(\omega, \delta)$ are lowered by the same amount with respect to $f_{co,ss}$ and $R_{c,ss}(\omega, \delta)$, while the inductance variation stays constant for both materials, i.e. $L_{c,alu}(\omega \to \infty, \delta) = L_{c,ss}(\omega \to \infty, \delta)$. It should be added that in contrast to the simple transformer equivalent model, the FEM simulation also considers the AC resistance of the targets, which is the reason why the resistances are not settling to the aforementioned values for high frequencies. For materials with high conductivity, this effect is more pronounced, which means it results in a larger scaling R_{AC}/R_{DC} at a given frequency. Furthermore, above a certain frequency this also negatively affects the resistance variation. In general, as a rule of thumb, it can be stated that for a given ECS geometry the target material and thickness should be selected such that f_{co} is located at least one decade below the desired excitation frequency f_{exc}, e.g. defined by the needed sensor bandwidth, in order to obtain the highest position sensitivity.

III. ECS MEASURING THROUGH A CONDUCTIVE SURFACE

Consider now the configuration of **Fig. 4 (a)**, where based on the underlying application the excitation coil is located inside the sealed stator, i.e. behind a *stationary shield* with conductivity σ_s and relative permeability $\mu_{r,s}$, and thus the distance δ between shield and moving target has to be sensed. As for the target, in the following a relative permeability of $\mu_{r,s} \approx 1$ is assumed for the shield.

Since now the excitation coil is almost directly attached to the conductive shield, the magnetic coupling between coil and shield is typically much higher than the one between coil and target, especially in cases where the target is located at a large distance δ. Hence, starting from the case without any target, i.e. $\delta \to \infty$, where only the shield layer is in close proximity to the excitation coil, the shield acts like a target for the conventional ECS discussed in **Sec. II**. This means that ± 1 decade around the cutoff frequency - now defined by the shield's R_s and L_s as $\omega_{co,s} = 2\pi f_{co,s} = R_s/L_s$ - the coil input resistance and inductance increases/decreases by the amount given in (4) and (5), respectively. As mentioned, since the shield is closely attached to the coil (there is no offset of $0.5\,mm$ as considered for the targets of the conventional ECS), the magnetic coupling $k(\omega, \delta)$ is increased, resulting in a larger coil resistance and inductance variation around $\omega_{co,s}$. This is highlighted in **Fig. 3**, where in addition to the previous targets also the resulting coil resistances and inductances for shields made of $0.5\,mm$ stainless steel ($\sigma_{ss} = 1.45\,MS\,m^{-1}$) and aluminum ($\sigma_{alu} = 37.7\,MS\,m^{-1}$) are shown. As can be noticed, in order to achieve a high impedance variation, i.e. measurement sensitivity, a shield layer with high R_s must be selected. This is also clear from the fact that with a lower R_s, larger eddy currents are induced in the shield, and thus the remaining flux linked with the target is small.
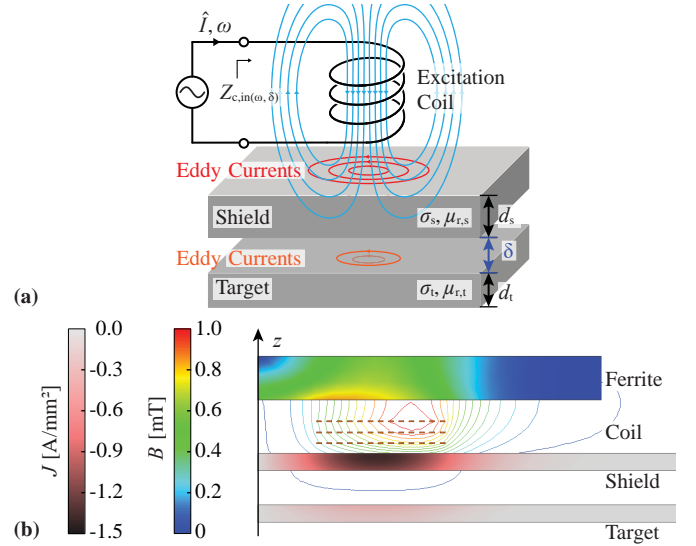
Fig. 4: (a) Planar single-coil ECS measuring the distance δ between the stationary intermediate conductive shield and the moveable conductive target. **(b)** ECS arrangement used for the axisymmetrical 2D FEM simulations (ANSYS) with exemplary field and current distribution for a $0.5\,mm$ stainless steel shield/target combination at an excitation frequency of $f_{exc} = 430\,kHz$.

TABLE II: Different material and thickness combinations.

Design Name	Shield Material	Shield Thickness	Target Material	Target Thickness
D1	Stainless Steel	0.5 mm	Aluminum	0.5 mm
D2	Stainless Steel	0.2 mm	Aluminum	0.5 mm
D3	Stainless Steel	0.5 mm	Stainless Steel	0.5 mm
D4	Stainless Steel	0.2 mm	Stainless Steel	0.5 mm

If now a target is approaching the shield, the magnetic coupling to the target is increasing and additional eddy currents are induced in the target. At the coil terminals this is noticed as a reduction of the input impedance, where the variation is intensified with lower R_t. Hence, for an ECS measuring through a shield, the resistance R_t shown in the equivalent circuit of **Fig. 2 (b)** for the conventional ECS, could be substituted by some equivalent resistance R_{eq}, which is a sort of a parallel combination of R_s and R_t, however, where also the distance- and frequency-dependent couplings between coil, shield and target has to be considered. In other words, R_{eq} can also be seen as some special target at some equivalent position having some mixed material properties of shield and target.

Nevertheless, independently from the exact value R_{eq}, this means that the impedance curve measured with only the shield (cf. **Fig. 3**), continuously decays if a target approaches the shield. Furthermore, as R_{eq} is smaller for closer targets, also the cutoff frequency is shifted to lower frequencies. Unfortunately, the amount of reduction depends on the ratio of R_s and R_t as well as on their magnetic couplings to the coil, which are difficult to calculate. However, if for the extreme case $\delta = 0\,mm$ it is assumed that the shield and target have the same coupling to the coil, then the minimum cutoff frequency is roughly given by the parallel connection of R_s and R_t as

$$\omega_{co,min} = 2\pi f_{co,min} = R_s R_t/(R_s + R_t)/L_s. \quad (6)$$

Consequently, in cases where the target has a much higher conductivity than the shield, $\omega_{co,min}$ is much lower than $\omega_{co,s}$, while for equal shield and target resistances, $\omega_{co,min}$ is roughly $\omega_{co,s}/2$.

A. Impedance Variation obtained by FEM Simulations

The described behavior is verified in **Fig. 5**, which shows the simulated resistance and inductance curves for the distances $\delta = 0\,mm$, $1\,mm$, $2\,mm$ and $\delta \to \infty$ (i.e. only the shield) as well as for different material and thickness combinations as summarized in **Tab. II**. The impedance curves are again obtained from FEM simulation, where the arrangement of **Fig. 4 (b)** is used.
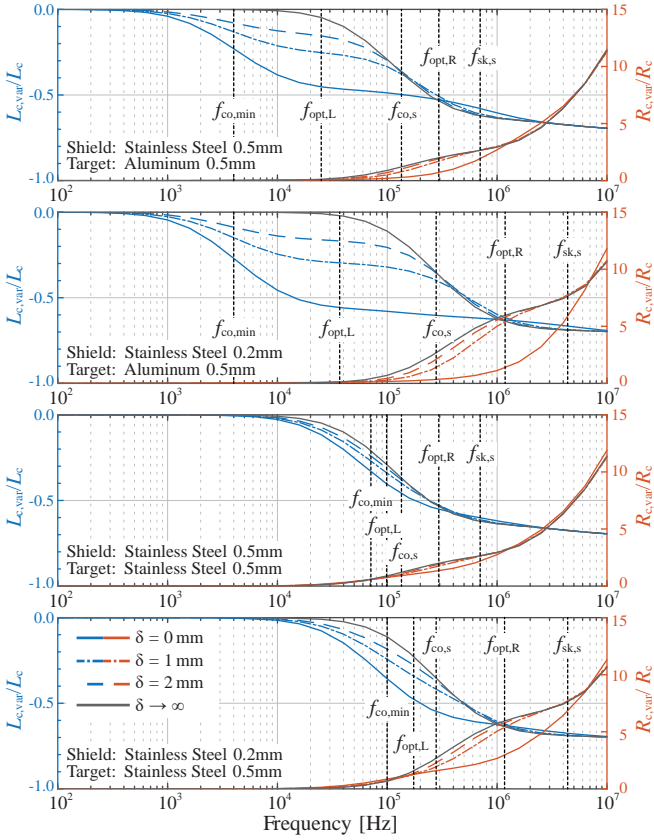
Fig. 5: Normalized $R_{c,var}(\omega,\delta)$ and $L_{c,var}(\omega,\delta)$ versus frequency for the designs listed in **Tab. II** at $\delta = 0\,\text{mm}$, $1\,\text{mm}$, $2\,\text{mm}$ and $\delta \to \infty$ (i.e. only shield), as obtained from FEM simulations. The obtained values of R_c and L_c are $2.8\,\Omega$ and $13.9\,\mu\text{H}$, respectively. The cutoff frequency f_{co}, the skin depth related frequency of the shield $f_{sk,s}$ and the optimal excitation frequencies $f_{exc,opt,R}$ and $f_{exc,opt,L}$ are also indicated (cf. **Tab. III**).

As can be noticed, for the design **D1** with a highly resistive stainless steel shield and a highly conductive aluminum target a large impedance variation is obtained. Above f_{co} a strong resistance variation is visible, because R_{eq} is highly influenced by the low $R_{t,alu}$. Furthermore, a low $R_{t,alu}$ leads to a wide shift of f_{co} to $f_{co,min}$ and thus to a large inductance variation. In cases where also from manufacturability perspective the shield thickness can be further reduced (cf. design **D2**), the resistance and inductance sensitivity is enhanced. It has to be considered that due to the 2.5 times higher $R_{s,ss}$ also f_{co} increases by the same amount, while $f_{co,min}$ - mainly defined by $R_{t,alu}$ - stays almost the same. In design **D3**, for shield and target the same material and thickness are used and the resistance variation again takes place above f_{co}, but it is much smaller because the high resistive target $R_{t,ss}$ has a much lower influence on R_{eq}. Clearly, also the frequency shift from f_{co} to $f_{co,min}$ is smaller, which as stated above is less than $f_{co}/2$, thus the inductance variation is limited. Similar to design **D2**, also in case of equal materials, a thickness reduction of the shield improves the sensitivities (cf. design **D4**). Again, f_{co} is increased by 2.5 due to the 2.5 times higher $R_{s,ss}$.

As can be noticed for all designs, above a certain frequency, the skin and proximity effects of the shield become dominant and hinder the magnetic field to pass the shield layer, i.e. the target position sensitivity is lost. Consequently, f_{exc} must stay below a certain *skin depth related* frequency $f_{sk,s}$ of the shield, deduced from the skin depth $\delta_{sk,s}$ where it is assumed that $\delta_{sk,s} = d_s$, given as

$$\delta_{sk,s} = \sqrt{\frac{1}{\pi\mu_0\mu_{r,s}\sigma_s f}} \quad \to \quad f_{sk,s} = \frac{1}{\pi\mu_0\mu_{r,s}\sigma_s d_s^2}. \tag{7}$$

TABLE III: Characteristic and optimal excitation frequencies.

	D1	**D2**	**D3**	**D4**	Unit
$f_{co,min}$	4	4	71	100	[kHz]
$f_{co,s}$	126	282	126	282	[kHz]
$f_{sk,s}$	699	4367	699	4367	[kHz]
$f_{exc,opt,R}$ (calc)	297	1109	297	1109	[kHz]
$f_{exc,opt,L}$ (calc)	24	35	94	168	[kHz]
$f_{exc,opt,R}$ (FEM)	316	1259	430	1122	[kHz]
$f_{exc,opt,L}$ (FEM)	25	45	89	178	[kHz]

B. Optimal Excitation Frequencies

As can be noticed from **Fig. 5**, for all designs the maximum resistance variation $\Delta R_{c,var}(f_{exc,opt,R},\delta)$ and inductance variation $\Delta L_{c,var}(f_{exc,opt,L},\delta)$ occur in different frequency ranges and thus at different optimal excitation frequencies $f_{exc,opt,R}$ and $f_{exc,opt,L}$ as listed in **Tab. III**. Furthermore, as stated above, the frequency range of the resistance variation is roughly defined by $f_{co,s}$ and $f_{sk,s}$, while the inductance variation is limited to a lower frequency range given by $f_{co,min}$ and $f_{co,s}$. As a rule of thumb, assuming that the optimal excitation frequency has to be located symmetrically within these boundaries, i.e. the geometric mean, the optimal excitation frequencies for the resistance and inductance variation can be roughly calculated as

$$f_{ext,opt,R} \approx \sqrt{f_{sk,s} \cdot f_{co,s}}, \quad f_{ext,opt,L} \approx \sqrt{f_{co,min} \cdot f_{co,s}}. \tag{8}$$

As can be noticed from **Tab. III**, the calculated optimal excitation frequencies based on (8) are in good agreement with the optimal excitation frequencies obtained from **Fig. 5**. The discrepancy between FEM simulation and calculation is within 10%, only $f_{ext,opt,L}$ of design **D2** differs by 20% and $f_{ext,opt,R}$ of design **D3** differs by 30%. However, even if for **D3** the calculated frequency is selected, the max. resistance variation decreases by only 13%.

C. General ECS Design Guidelines

Summarizing, from the FEM results and the considerations above it is possible to provide the following guidelines:

- In order to achieve a high measurement sensitivity, for both resistance and inductance variation, the shield resistance R_s should be much larger than the target resistance R_t, which is either obtained by selecting different materials or by using different thicknesses.
- A large shield resistance R_s increases both the cutoff frequency $f_{co,s}$ and the skin depth related frequency $f_{sk,s}$, resulting in a larger measurement bandwidth.
- The resistance variation starts around $f_{co,s}$ and ends around $f_{sk,s}$, which are both defined by only the shield layer.
- The range of inductance variation is defined by $f_{co,min}$ and $f_{co,s}$.
- The optimal excitation frequency is roughly calculated with (8), which is the geometric mean of the frequency boundaries.

IV. EXPERIMENTAL SETUP

A. PCB-embedded Excitation Coil Design

In general, the excitation coil has to be designed in such a way that on one hand, based on (4) and (5), a maximum impedance variation is achieved, and on the other hand this impedance variation caused by the target is not affected by the coil impedance itself, i.e. for example a strongly increasing AC resistance or a low coil self-resonance frequency.

A maximum impedance variation is obtained with a large self-inductance L_c, which in general means a maximum diameter and maximum number of turns. For the underlying application, the outer diameter of the coil (also a square coil shape would be possible) is limited to $d_{c,out} = 11.5\,\text{mm}$, while based on [15] the inner diameter should not be smaller than $d_{c,in} = 3\,\text{mm}$, since the most inner turns don't enlarge the inductance noticeably but lead to a larger high-frequency coil resistance and lower quality factor. With the given PCB design constraints like minimum track width and distance of $150\,\mu\text{m}$, the maximum number of turns per layer is
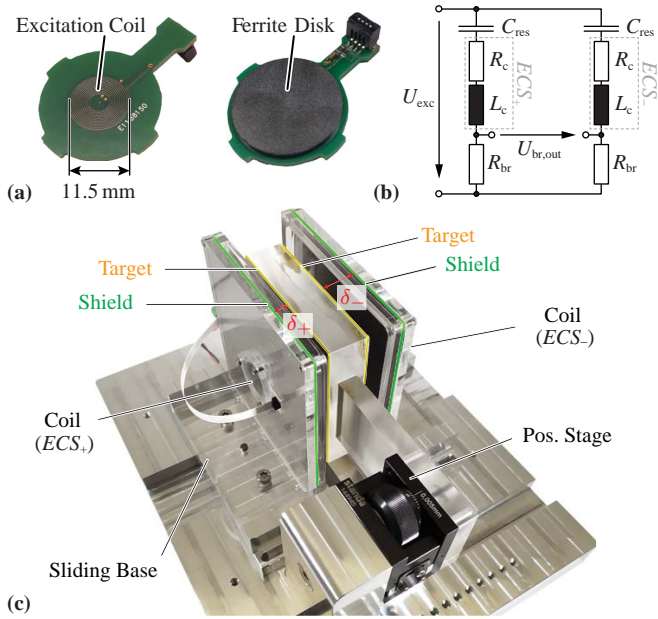
Fig. 6: **(a)** Realized PCB-embedded excitation coil. **(b)** Wheatstone bridge used to implement the ECS as a differential sensor. The capacitors C_{res} are used to match the series resonance to the excitation frequency. **(c)** Realized mechanical test bench used to verify the differential ECS concept.

found as $N = 13$. The resulting self-inductance of a single-layer excitation coil is calculated as described in [16]–[20] and can be further increased if multiple layers of the PCB are used. In order to obtain the overall self-inductance, the magnetic coupling between the different layers has to be considered as given in [17], [18], [20]. In addition, a high-frequency ferrite core can be added on top of the coil to further increase L_c and the magnetic coupling. However, besides maximizing L_c, it always must be ensured that the coil's self-resonance frequency stays well above the desired excitation frequency range. Hence, the parasitic coil capacitance $C_{c,p}$ - mainly consisting of the inter-winding and inter-layer capacitances as well as the capacitance to the core - must be small. There, especially the inter-layer capacitances lead to a strong increase of $C_{c,p}$, and in order to keep the coil's self-resonance frequency above $10\,\text{MHz}$, i.e. around one decade above f_{exc}, three layers are selected. A picture of the realized PCB-embedded excitation coil is shown in **Fig. 6 (a)**.

B. Differential Sensor Configuration

According to **Tab. III**, the optimal excitation frequencies for inductance variation $f_{exc,opt,L}$ are considerably smaller than the ones for resistance variation $f_{exc,opt,R}$. Therefore, in order to achieve a sufficient measurement bandwidth for the underlying application, the resistance variation $\Delta R_{c,var}(f_{exc,opt,R}, \delta)$ is measured. Furthermore, since the nominal mover position is at $\delta = 1\,\text{mm}$, and the position sensor should only output a voltage if the mover is displaced, for the measurement of the x- and y-displacement two identical ECS ECS_+ and ECS_- are placed on opposite sides of the rotor, which are then used as a differential sensor in a *Wheatstone bridge* configuration (cf. **Fig. 6 (b)**) as proposed in [21]–[23]. This also eliminates any thermal drifts and dependencies of $\Delta R_{c,var}(f_{exc,opt,R}, \delta)$, and only leads to a temperature-dependent sensitivity, which can be compensated by measuring e.g. the stator temperature.

C. Mechanical Test Bench

Fig. 6 (c) shows the mechanical test bench used to verify the results obtained from the FEM simulations. It consists of two rigid plastic frames on which the $100\,\text{mm} \times 100\,\text{mm}$ shield samples and the PCB-embedded coil are mounted. In between them, a pair of square-shaped $80\,\text{mm} \times 80\,\text{mm}$ target samples of the same kind is glued on the two faces of a non-conductive support of thickness $10\,\text{mm}$,
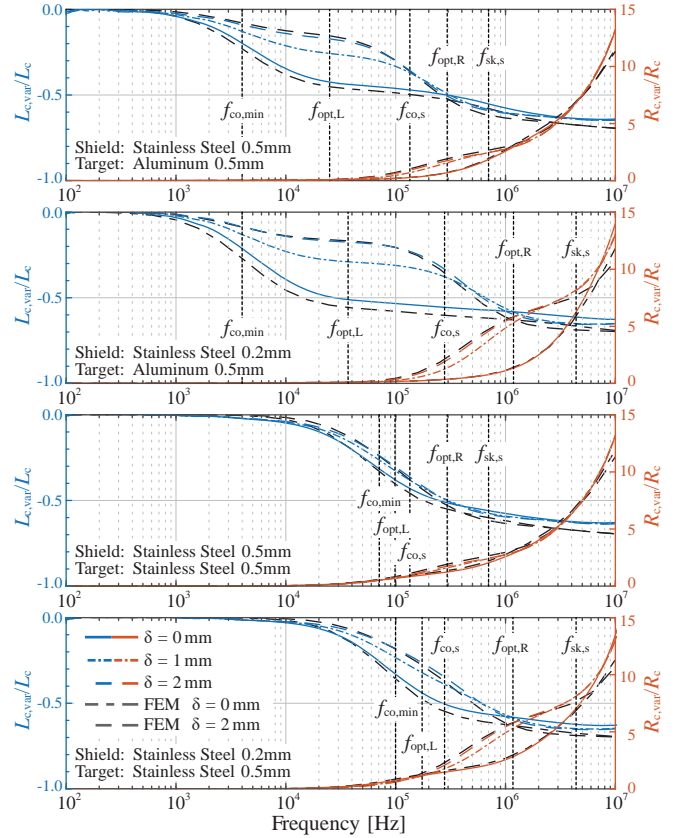
Fig. 7: Normalized $R_{c,var}(\omega, \delta)$ and $L_{c,var}(\omega, \delta)$ versus frequency for the designs listed in **Tab. II** at $\delta = 0\,\text{mm}$, $1\,\text{mm}$ and $2\,\text{mm}$, as obtained from impedance measurements. For a direct comparison, also the FEM results for the cases $\delta = 0\,\text{mm}, 2\,\text{mm}$ are reported (black dashed lines) and the frequencies of interest (cf. **Tab. III**) are indicated.

which is screwed to a precise positioning stage with a resolution of $5\,\mu\text{m}$ to move the target within the preferred distance range.

V. MEASUREMENTS AND RESULTS

A. Impedance Verification

First of all an impedance verification is performed, where the coil input impedances of a single-coil ECS is measured with the *Omicron Lab Bode 100* vector network analyzer for different distance δ and shield-target combinations (cf. **Tab. II**). The resulting resistance and inductance variations are reported in **Fig. 7** for the same distances $\delta = 0\,\text{mm}$, $1\,\text{mm}$ and $2\,\text{mm}$ as considered in **Fig. 5**. In order to enable a better comparison between the four cases, the variable resistance and inductance parts are again normalized to their DC values. Furthermore, for a direct comparison, also the results of the FEM simulations for the two boundary cases $\delta = 0\,\text{mm}$ and $2\,\text{mm}$ are shown. It can be noticed that in all cases the FEM simulations and measurements show an excellent correspondence with respect to frequency ranges and also relative variation.

B. Differential Bridge Output

In a second step, the sensitivity of the different designs (cf. **Tab. II**) is quantified by measuring the output voltage of the Wheatstone bridge, which is excited with a square wave signal between $0\,\text{V}$ and $U_{DC} = 5\,\text{V}$. Furthermore, for each design the optimal excitation frequency is selected and the series resonance capacitor C_{res} is adjusted in such a way that the resonance frequency matches with $f_{exc,opt,R}$, resulting in a quasi purely sinusoidal excitation current. There, both bridge legs are precisely tuned with a capacitive trimmer such that for the nominal (center) position, i.e. distance $\delta = 1\,\text{mm}$ measured from both ECSs placed on the opposite sides, the bridge output voltage $\hat{U}_{br,out}$ is practically zero. Furthermore, it should be considered that
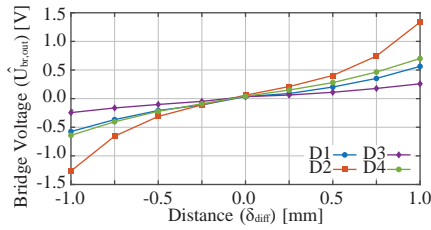
Fig. 8: Peak-to-peak amplitude of the bridge output voltage $\hat{U}_{\text{br,out}}$ versus displacement from the center position δ_{diff} for the designs listed in **Tab. II**.

TABLE IV: Wheatstone bridge parameters and measured sensitivities.

	D1	**D2**	**D3**	**D4**	Unit
$f_{\text{exc,opt,R}}$	297	1109	297	1109	[kHz]
C_{res}	43	3.3	26	3.3	[nF]
R_{br}	10	15	10	15	[Ω]
Sensitivity	0.464	0.897	0.236	0.558	[mV/μm]
Non-linearity	2.89	11	1.21	2.90	[%]

$\hat{U}_{\text{br,out}}$ also depends on the value of the bridge resistor R_{br}. Given the minimum and maximum measured values of $R_{\text{c,in}}$, it can be shown that an optimum value of R_{br} which maximizes $\hat{U}_{\text{br,out}}$ exists. The selected values of C_{res} and R_{br} for the considered designs are reported in **Tab. IV**. **Fig. 8** shows the measured $\hat{U}_{\text{br,out}}$ for each of the designs of **Tab. II** with respect to δ_{diff}, which corresponds to the displacement from the center position. The sensor output can be characterized with two main parameters, namely its *sensitivity* and *percentage non-linearity*. The former is directly computed by dividing the measured values of $\hat{U}_{\text{br,out}}$ by the corresponding value of δ_{diff} and averaging the results. The latter is usually given in percentage as $(err_{\text{abs,max}}/\text{FS}) \cdot 100\%$, where $err_{\text{abs,max}}$ is the maximum absolute error between the measured data and its best linear fit, and FS is the full scale of the sensor, which in this case is $2\,\text{mm}$ for each ECS. The achieved values are also reported for each design in **Tab. IV**. As already expected from the measured impedance variations, in **Fig. 8**, design **D2** with a thin shield and a highly conductive target offers the largest sensitivity of about $0.9\,\text{mV}\,\mu\text{m}^{-1}$. Design **D1** and **D4** feature similar sensitivities which are already roughly half of design **D2**. However, design **D4** has a 4 times higher optimal excitation frequency than **D1**, and thus enables also a larger measurement bandwidth. Finally, design **D3** has the lowest sensitivity and also the lowest bandwidth, i.e. both almost 4 times smaller than in design **D2**. Furthermore, it can be noted that a larger sensitivity results in a higher non-linearity. Based on these considerations, the most suitable design for the targeted application would be design **D2**, however, for a pure stainless steel housing, design **D4** is a good alternative offering a only ≈ 1.6 times lower sensitivity but improved non-linearity, while the achievable bandwidth is the same as with aluminum. Furthermore, it also has advantage in terms of manufacturability in industrial applications, and can be even preferred to aluminum for its properties, corrosion resistance and sterilizability.

VI. CONCLUSION

This paper investigates the design of an eddy current sensor (ECS) measuring the position of a moving conductive target located behind another fixed conductive shield. The performed FEM simulations allow to characterize the position-dependent resistance and inductance variations measured at the excitation coil terminals versus frequency for different combinations of shield and target materials and/or thicknesses. In addition, design guidelines are provided to select the optimal excitation frequencies based solely on the properties of the shield and target materials. The analysis is verified with measurements on a sensor prototype, showing that the frequency selection guidelines are valid. For the best case of a $0.2\,\text{mm}$ thick stainless steel shield and $0.5\,\text{mm}$ thick aluminum target, a sensitivity of up to $0.9\,\text{mV}\,\mu\text{m}^{-1}$ for a measuring range of $2\,\text{mm}$ with a sensor measurement bandwidth in the order of $100\,\text{kHz}$ can be achieved in

a differential configuration. Therefore, the sensor is applicable for active control of MBs.

REFERENCES

[1] A. J. Fleming, "A Review of Nanometer Resolution Position Sensors: Operation and Performance," *Sensors and Actuators A: Physical*, vol. 190, pp. 106–126, 2013.

[2] C. Huai-ning, "An Investigation of Microweighing with an Eddy Current Transducer," *Review of Scientific Instruments*, vol. 59, no. 10, pp. 2297–2299, 1988.

[3] X. Xue, Y. Dong, and X. Wu, "Motion Induced Eddy Current Sensor for Non-Intrusive Vibration Measurement," *IEEE Sensors Journal*, vol. 20, no. 2, pp. 735–744, 2019.

[4] J. Boehm, R. Gerber, and N. R. C. Kiley, "Sensors for Magnetic Bearings," *IEEE Transactions on Magnetics*, vol. 29, no. 6, pp. 2962–2964, Nov. 1993.

[5] L. Xi'nan, W. Fengxiang, and W. Baoguo, "Application of Eddy-Current Sensor for Air Gap Detection in Magnetic Suspension Motors," in *Proc. of the 5th International Conference on Electrical Machines and Systems (ICEMS, IEEE Cat. No. 01EX501)*, vol. 1, pp. 326–329. IEEE, 2001.

[6] S. Miric, R. Giuffrida, D. Bortis, and J. Kolar, "Dynamic Electromechanical Model and Position Controller Design of a New High-Precision Self-Bearing Linear Actuator," *IEEE Transactions on Industrial Electronics*, pp. 1–1, 2020.

[7] A. Sophian and M. Fan, "Pulsed Eddy Current Non-destructive Testing and Evaluation: A Review," *Chinese Journal of Mechanical Engineering*, vol. 30, pp. 1474–1474, 11 2017.

[8] S. D. Roach, "Designing and Building an Eddy Current Position Sensor," *Sensors - The Journal of Applied Sensing Technology*, vol. 15, no. 9, pp. 56–74, 1998.

[9] D. J. Sadler and C. H. Ahn, "On-chip Eddy Current Sensor for Proximity Sensing and Crack Detection," *Sensors and Actuators A: Physical*, vol. 91, no. 3, pp. 340–345, 2001.

[10] M. Jagiella, S. Fericean, and A. Dorneich, "Progress and Recent Realizations of Miniaturized Inductive Proximity Sensors for Automation," *IEEE Sensors Journal*, vol. 6, no. 6, pp. 1734–1741, 2006.

[11] M. R. Nabavi and S. N. Nihtianov, "Design Strategies for Eddy-Current Displacement Sensor Systems: Review and Recommendations," *IEEE Sensors Journal*, vol. 12, no. 12, pp. 3346–3355, 2012.

[12] S. Shokralla, S. Sullivan, J. Morelli, and T. W. Krause, "Modelling and Validation of Eddy Current Response to Changes in Factors Affecting Pressure Tube to Calandria Tube Gap Measurement," *NDT&E International*, vol. 73, pp. 15 – 21, 2015.

[13] C. V. Dodd and W. E. Deeds, "Analytical Solutions to Eddy-Current Probe-Coil Problems," *Journal of Applied Physics*, vol. 39, no. 6, pp. 2829–2838, 1968.

[14] C. V. Dodd, W. E. Deeds, J. W. Luquire, and W. Spoeri, "Some Eddy-Current Problems and their Integral Solutions," Oak Ridge National Laboratory, Tech. Rep. W-7505-eng-26, Apr. 1969.

[15] C. Oberhauser, "LDC Sensor Design," Texas Instruments, Tech. Rep. SNOA930B, Mar. 2015.

[16] S. S. Mohan, M. del Mar Hershenson, S. P. Boyd, and T. H. Lee, "Simple Accurate Expressions for Planar Spiral Inductances," *IEEE Journal of Solid-State Circuits*, vol. 34, no. 10, pp. 1419–1424, 1999.

[17] S. Asgaran, "New Accurate Physics-based Closed-form Expressions for Compact Modeling and Design of On-Chip Spiral Inductors," in *Proc. of 14th International Conference on Microelectronics*, pp. 247–250, 2002.

[18] J. Zhao, "A New Calculation for Designing Multilayer Planar Spiral Inductors," *EDN (Electrical Design News)*, vol. 55, no. 14, p. 37, 2010.

[19] A. B. Islam, S. K. Islam, and F. S. Tulip, "Design and Optimization of Printed Circuit Board Inductors for Wireless Power Transfer System," *University of Tennessee - Faculty Publications and Other Works – EECS*, 04 2013.

[20] P. K. Chawda, "An Automated Design Flow for Synthesis of Optimal Multi-layer Multi-shape PCB Coils for Inductive Sensing Applications," in *Proc. of 19th International Symposium on Quality Electronic Design (ISQED)*, pp. 290–295, 2018.

[21] H. Wang and Z. Feng, "Ultrastable and Highly Sensitive Eddy Current Displacement Sensor Using Self-temperature Compensation," *Sensors and Actuators A: Physical*, vol. 203, pp. 362 – 368, 2013.

[22] H. Wang, Y. Liu, W. Li, and Z. Feng, "Design of Ultrastable and High Resolution Eddy-Current Displacement Sensor System," in *Proc. of 40th Annual Conference of the IEEE Industrial Electronics Society (IECON)*, pp. 2333–2339, 2014.

[23] R. Pallas-Areny and J. Webster, *Sensors and Signal Conditioning, 2nd Edition*. John Wiley and Sons, 01 2001.